Supplementary Information for

Diffusioosmotic and convective flows induced by a non-electrolyte concentration gradient

Ian Williams, Sangyoon Lee, Azzurra Apriceno, Richard P. Sear and Giuseppe Battaglia

Ian Williams
E-mail: iwilliams@ibecbarcelona.eu

This PDF file includes:

Supplementary text
Figs. S1 to S13
SI References

Supporting Information Text

Velocity Profiles Do Not Depend On Waiting Time

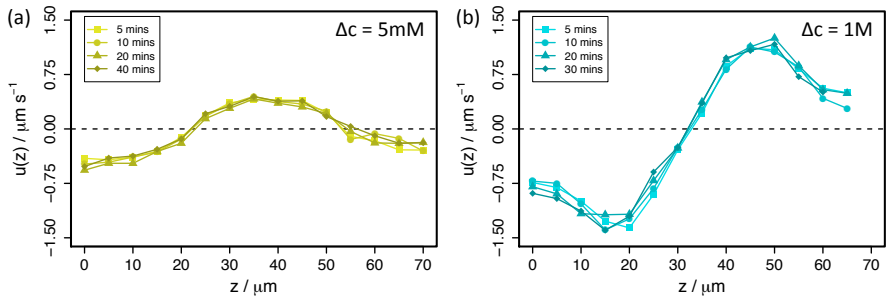

Fig. S1. Experimentally measured velocity profiles in glucose gradients formed between reservoirs at $c = 0$ and $c = \Delta c$ after waiting times indicated in legend in (a) $5\,\mathrm{mM/mm}$ gradient and (b) $1\,\mathrm{M/mm}$ gradient.

Figure S1 shows experimentally measured velocity profiles in experiments in which a glucose gradient is established between water and reservoirs at concentrations 5 mM (a) and 1 M (b). In each plot, four profiles are shown corresponding to different waiting times after initialising the experiment. In both gradients, the four profiles fall on top of one another, suggesting that the velocity profile is independent of time between 5 and 40 minutes after initiation, and thus that the concentration gradient is quasistatic on this timescale. This reinforces the findings of the COMSOL model described in Materials and Methods. Based on this, we neglect time since initiation as a variable, and directly compare all measurements made after different waiting times.

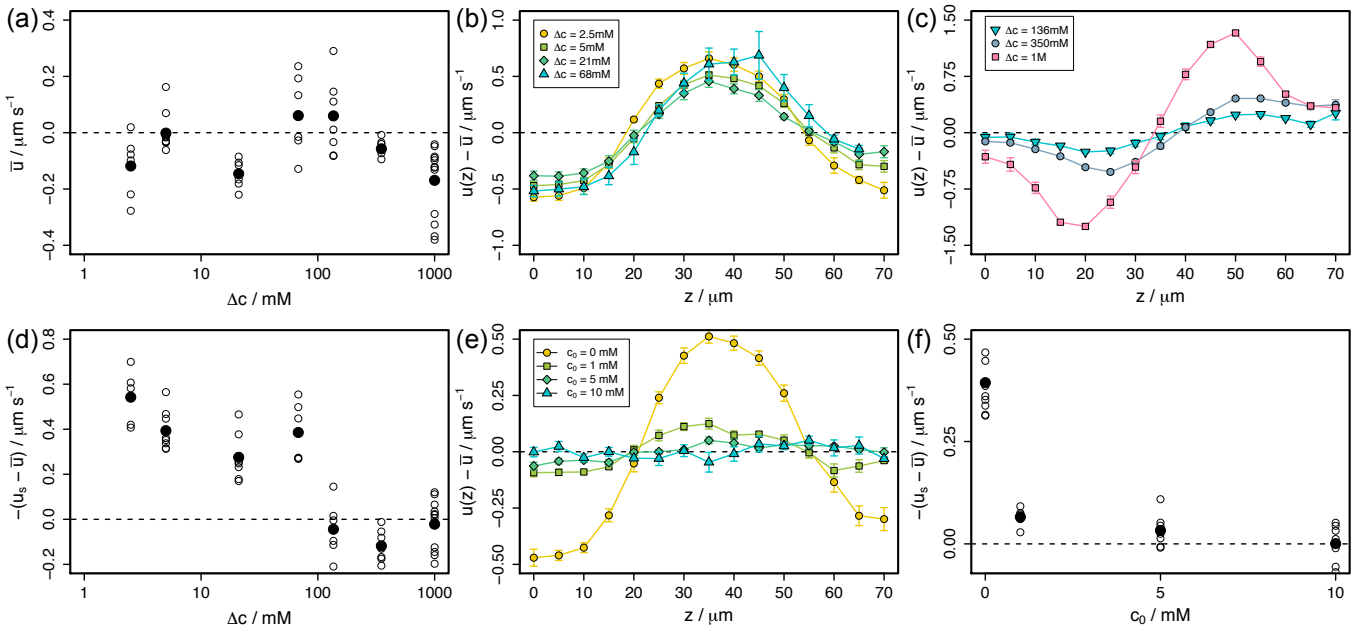

Fig. S2. (a) z-averaged velocities as a function of concentration drop over the gradient channel for experiments in glucose gradients established between reservoirs at $c = 0$ and $c = \Delta c$. Open points are individual experiments and solid points show the average over all experiments at each Δc. (b,c) Average velocity profiles offset by net velocities shown in (a) for experiments with reservoirs at $c_0 = 0$ and Δc indicated in legends. (d) Estimated slip velocities, offset by net velocities, measured in experiments in (b) and (c). (e) Average velocity profiles offset by net velocities for experiments with reservoirs at c_0 and $c_0 + 5\,\mathrm{mM}$, with c_0 indicated in the legend. (f) Estimated slip velocities, offset by net velocities, measured in experiments in (e).

Diffusioosmotic flows along the particle surface can drive diffusiophoretic particle motion relative to the fluid. Diffusiophoretic motion of the tracer particles should not depend on the vertical position of the particle in the gradient channel and would therefore present as a vertical offset in the velocity profiles. In order to check for this motion, the spatially averaged tracer velocity, $\bar{u} = (1/H)\int_0^H u(z)\,dz$, is calculated for each experiment and plotted in Fig. S2 (a). Open symbols show $\bar{u}$ in individual experiments while solid points represent $\bar{u}$ calculated using the average profiles shown in the main text.

There is no consistent net tracer motion, with $\bar{u}$ distributed around zero, and no obvious trend to these data. Although we expect DP to contribute to tracer motion, these data reveal neither its magnitude (which likely depends on Δc) nor its direction. In nominally identical experiments, a range of net velocities are measured. This range often includes both positive and negative net velocities. Diffusiophoretic tracer motion is anticipated to at least be consistent in its direction, either up or down the glucose gradient. These data suggest that DP does not make an important contribution to our measurements. We believe that the observed ranges of net velocity represent the statistical variation between repeated experiments of finite duration in which Brownian motion remains an important influence on tracer dynamics. Any DP velocity is likely masked by these variations and therefore challenging to discern. Therefore, in the main manuscript we disregard DP as a contributor to tracer motion. However, it is possible that if fluid flows can be suppressed, DP may be observed, as it has been for similar particles in sucrose gradients (1). It is important to note that since our data suggest that DO speeds do not depend on the concentration gradient in a simple way, it is reasonable to assume that DP speeds also exhibit a non-trivial scaling.

However, we could choose to interpret the net velocity in each experiments as a DP velocity. In that case, the true fluid velocity profile is the measured velocity profile offset by the net velocity, $u(z) - \bar{u}$. These offset velocity profiles are shown in Fig. S2 (b), (c) & (e), which should be compared to Fig. 3 (a) & (b) and Fig. 4 (a) in the main manuscript respectively. The corresponding estimated slip velocities offset by the net velocities are shown in Fig. S2 (d) and (f), which are analogous to main manuscript Fig. 3 (c) and Fig. 4 (b). Accounting for potential DP in this way has no effect on the qualitative features of these data and only a very small quantitative effect. The interpretation and conclusions of this research remain unchanged when the data are offset by the net velocity in each experiment, as it is the shapes of the velocity profiles that inform our interpretations, not their magnitudes.

No Tracer Motion Without Glucose

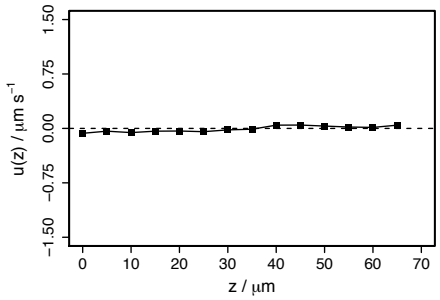

Fig. S3. Velocity profile measured in experiment with $c = 0$ in both reservoirs.

To ensure that measured velocity profiles are due to the presence of a glucose gradient, we performed an experiment in which both reservoirs are loaded with a suspension of tracer particles in water without glucose. The measured velocity profile is shown in Fig. S3. In the absence of a glucose gradient, no circulating fluid flow is observed, and we therefore surmise that flow measured in glucose gradients is due to the presence of glucose and not due to the protocol by which the sample chamber is loaded.

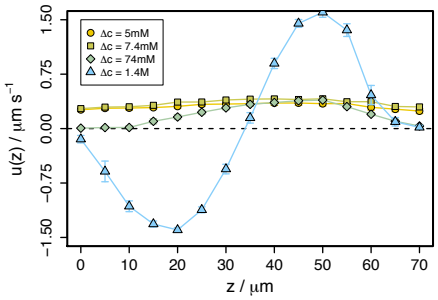

Fig. S4. Tracer velocity profiles measured in KCl gradients established between reservoirs at $c = 0$ and $c = \Delta c$ indicated in legend.

In gradients of the electrolyte potassium chloride (KCl), we measure tracer velocity profiles as shown in Fig. S4. The highest concentration $\Delta c = 1.4\,\mathrm{M}$ is chosen such that its density matches that of 1 M glucose. In this case, the velocity profile indicates buoyancy-driven convection, and directly overlays the velocity profile measured for 1 M glucose.

In smaller concentration gradients, rather than the parabolic profile observed in glucose gradients, indicative of flow driven primarily by a diffusioosmotic slip velocity at the channel walls, in KCl we instead measure a positive tracer velocity that is independent of z. Since the experimental sample chamber is sealed, net fluid motion in one direction is prohibited, and so the tracer particles must be moving with respect to the fluid. Therefore, we surmise that, in small electrolyte gradients, we observe significant diffusiophoretic motion of a polystyrene colloids. Diffusiophoretic motion of charged polystyrene colloids in electrolyte gradients has been observed by many researchers (1–5) and this DP motion is easily resolved in our experiments using KCl. This contrasts with our glucose experiments, where the velocity profiles show no consistent vertical offset indicative of particle diffusiophoresis.

Furthermore, these profiles show no evidence of a diffusioosmotic flow at the channel walls, in contrast with the glucose measurements presented in the main manuscript. In KCl we measure particle diffusiophoresis, but no channel wall diffusioosmosis and in glucose we measure the opposite: channel wall diffusioosmosis but no diffusiophoresis.

Glucose Solution Viscosity

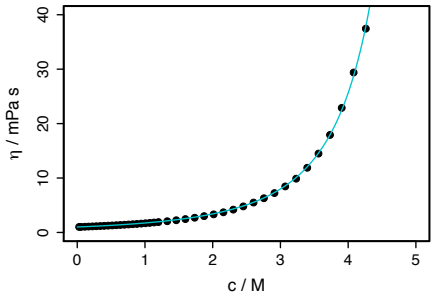

Fig. S5. Viscosity of glucose solutions as a function of concentration at $T = 20^\circ$ C. Black points are data from the CRC Handbook of Physics and Chemistry (6). Line shows fit to data.

To obtain the dependence of glucose solution viscosity on concentration, we fit data available in the CRC Handbook of Physics and Chemistry (6). These data are shown as black points in Fig. S5. The line shows our fit, given by

$$\eta = \eta_s \left(1 - c/6.2586\right)^{-3.1828}, \qquad [1]$$

where $\eta_s = 1.0002$ mPa (6) is the solvent viscosity at 293 K.

Model For Diffusioosmosis with Explicit Slip Length. We approximate the interfacial region as a slab of height $\lambda\sigma$ that is uniform in both the vertical direction and along the surface. We treat it as a slab of bulk solution. In particular, its viscosity is given by the fit to bulk data of Eq. (1).

As is conventional in studies of DP/DO, we assume that in the bulk the hydrostatic pressure has relaxed to a uniform value, p^{BULK} that is independent of x. However, the varying concentration along x means that the osmotic pressure varies along x. We write the hydrostatic pressure as the sum of a solvent contribution to the pressure and an osmotic pressure (7, 8)

$$p^{\mathrm{BULK}} = p_{\mathrm{s}}^{\mathrm{BULK}}(x) + \Pi^{\mathrm{BULK}}(x) \tag{2}$$

with $p_{\mathrm{s}}^{\mathrm{BULK}}(x)$ the contribution of the solvent to the pressure and $\Pi^{\mathrm{BULK}}(x)$ the bulk osmotic pressure due to the solute. The constant p^{BULK} implies that $\nabla p_{\mathrm{s}}^{\mathrm{BULK}} = -\nabla\Pi^{\mathrm{BULK}}$.

In the interfacial region, the hydrostatic pressure, p^{SL}, does vary with x, we have

$$p^{\mathrm{SL}}(x) = p_{\mathrm{s}}^{\mathrm{SL}}(x) + \Pi^{\mathrm{SL}}(x) \tag{3}$$

with $p_{\mathrm{s}}^{\mathrm{SL}}$ and Π^{SL} the solvent pressure and osmotic pressure in the interfacial layer, respectively. Flows are driven by gradients in the hydrostatic pressure, which are limited to the interface, *i.e.*, it is the gradients in p^{SL} that drive DO flows.

We further assume that the solvent pressure is the same in the surface layer as in the bulk at the same x due to local equilibrium of the solvent. This is a standard assumption in the theory of Derjaguin, Anderson and others (7–10). Equating surface and bulk solvent pressures, we obtain $\nabla p_{\mathrm{s}}^{\mathrm{SL}} = \nabla p_{\mathrm{s}}^{\mathrm{BULK}}$, and as $\nabla p_{\mathrm{s}}^{\mathrm{BULK}} = -\nabla\Pi^{\mathrm{BULK}}$,

$$\nabla p^{\mathrm{SL}} = \nabla p_{\mathrm{s}}^{\mathrm{SL}} + \nabla\Pi^{\mathrm{SL}} = \nabla\left(\Pi^{\mathrm{SL}} - \Pi^{\mathrm{BULK}}\right) \tag{4}$$

So, we have stress gradients (only) in the interfacial region. These drive flow, and to obtain the flow speed, we use the x-component of the Stokes equation, which is

$$\frac{\mathrm{d}^2 u_x}{\mathrm{d}z^2} = \begin{cases} \frac{1}{\eta_{\mathrm{g}}}\left(\frac{\partial p^{\mathrm{SL}}}{\partial x}\right) & 0 < z < \lambda\sigma \\ 0 & \lambda\sigma < z \end{cases} \tag{5}$$

Using Eq. (4) for the stress gradient in the interfacial region this becomes

$$\frac{1}{\eta_{\mathrm{g}}}\left(\frac{\partial p^{\mathrm{SL}}}{\partial x}\right) = \frac{\partial}{\partial x}\left(\Pi^{\mathrm{SL}} - \Pi^{\mathrm{BULK}}\right) = B \quad 0 < z < \lambda\sigma \tag{6}$$

which defines B. Then using Eq. (6) in Eq. (5), and integrating

$$u_x(z) = \begin{cases} \frac{1}{2}Bz^2 - B(\lambda\sigma)\,(b+z) & 0 < z < \lambda\sigma \\ -\frac{1}{2}B(\lambda\sigma)\,(\lambda\sigma + 2b) & \lambda\sigma < z \end{cases} \tag{7}$$

where we applied two boundary conditions. The first is a Navier boundary condition at the surface ($z = 0$) with a slip length b,

$$b\left(\frac{\mathrm{d}u_x}{\mathrm{d}z}\right)_{z=0} = u_x(z=0). \tag{8}$$

This is included for completeness and generality, but it is assumed that $b = 0$, corresponding to a no-slip boundary condition, $u_x(z=0) = 0$. The second condition is the continuity of the first derivative of u_x at the outside edge of the surface layer, $(\partial u_x/\partial z)_{z=\lambda\sigma} = 0$.

The DO speed, u_{DO}, is the speed outside the interface, at $z > \lambda\sigma$, which is

$$u_{\mathrm{DO}} = -\frac{1}{2\eta_{\mathrm{g}}}\left[\frac{\partial}{\partial x}\left(\Pi^{\mathrm{SL}} - \Pi^{\mathrm{BULK}}\right)\right]\Lambda^2 \tag{9}$$

using Eq. (6) for B and

$$\Lambda^2 = (\lambda\sigma)^2\left(1 + 2\frac{b}{\lambda\sigma}\right). \tag{10}$$

Treating both the bulk and interfacial regions as ideal solutions (e.g., $\Pi^{\mathrm{BULK}} = ckT$), the concentration in the surface layer coexisting with a bulk concentration c is

$$c_{\mathrm{SL}} = c\exp\left(-\epsilon/k_{\mathrm{B}}T\right). \tag{11}$$

and then we obtain the expression in the main text for the DO speed, but generalised to the case of a non-zero slip length. This is

$$\Gamma_{DO} = \frac{f_{\mathrm{MN}}\,k_{\mathrm{B}}T\left[\exp(-\epsilon/k_{\mathrm{B}}T) - 1\right]\Lambda^2}{2\eta_{\mathrm{g}}(c_{\mathrm{SL}})} \qquad c_{\mathrm{SL}} < c_{\max} \tag{12}$$

and $\Gamma_{DO} = 0$ for $c_{\mathrm{SL}} > c_{\max}$. A first order correction for non-ideality using data from Miyajima *et al.* (11) is provided below.

Dependence of Model Predictions on ϵ, λ and σ_ϵ

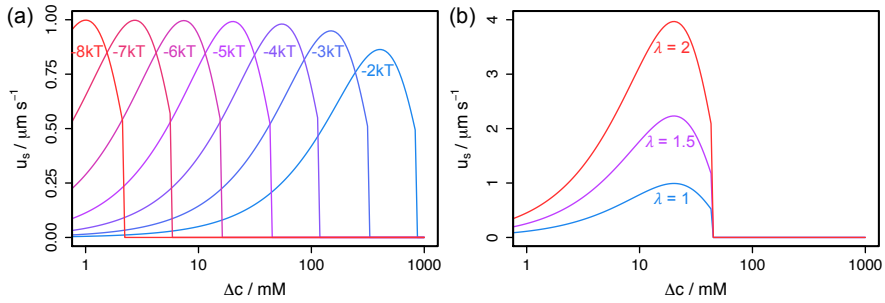

Fig. S6. Slip velocities in gradients established between $c_0 = 0$ and Δc predicted by homogeneously interacting model with (a) constant surface-solute interaction range, $\lambda = 1$, and varying interaction energy ϵ indicated by labels; and (b) constant interaction energy, $\epsilon = -5k_\mathrm{B}T$ and varying range λ.

Here we explore the dependence of the slip velocities predicted by our model on the parameters controlling the depth and range of the solute-surface interaction potential. We focus on the case of gradients established between $c_0 = 0$ and Δc. For the homogeneously interacting surface, these predictions are shown in Fig. S6 where (a) shows the effect of varying the interaction strength, ϵ at fixed range $\lambda = 1$ and (b) shows the effect of varying the interaction range, λ at fixed $\epsilon = -5k_\mathrm{B}T$.

All other parameters remaining constant, changing ϵ primarily shifts the curve horizontally in this representation. As the predicted slip velocity depends on the concentration in the interfacial region, increasing ϵ simply decreases the bulk concentration required for a given surface layer concentration. The magnitude of the predicted slip velocity, *i.e.* the peak height, is only very weakly dependent on ϵ, showing a small decrease as ϵ is decreased.

The scale of predicted slip velocities is much more sensitive to the range of the solute-surface interaction, as shown in Fig. S6 (b). The slip velocity scales with $(\lambda\sigma)^2$, and so doubling λ results in a four-fold increase in the predicted speeds.

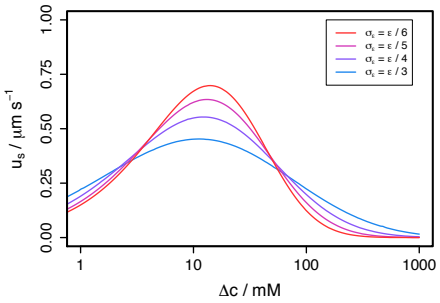

Fig. S7. Slip velocities in gradients established between $c_0 = 0$ and Δc predicted by heterogeneously interacting model with constant mean interaction energy $\bar{\epsilon} = -kk_\mathrm{B}T$ and varying standard deviation σ_ϵ indicated in legend.

Our model for heterogeneous surface-solute interactions depends on the average interaction strength, $\bar{\epsilon}$ and the standard deviation of the (Gaussian) distribution of interaction strengths, σ_ϵ. Altering $\bar{\epsilon}$ has the same effect as altering ϵ in the homogenous model. The effect of altering σ_ϵ is shown in Fig. S7. Increasing the standard deviation of the interaction strength distribution both broadens the peak in $u_s(\Delta c)$ and decreases its height. A narrower distribution represents a less heterogeneous surface, and so the predicted curve will tend towards the homogeneous shape as $\sigma_\epsilon \to 0$.

Increasing Viscosity in the Uniform Viscosity Model

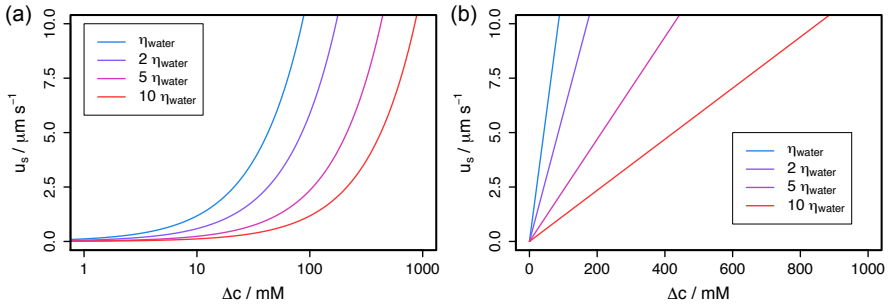

Fig. S8. The effect of varying viscosity on the slip velocities predicted by the uniform viscosity diffusioosmosis model of Derjaguin, Anderson, Prieve, Marbach and others (10, 12, 13) (equations 2 and 3 in the main article) for a linear concentration gradient formed between resevoirs at $c_0 = 0$ and Δc. Uniform viscosities are indicated in the legends. Data are shown with a logarithmic x axis in (a) and a linear x axis in (b). These data assume the same square-well-like solute-surface interaction of depth $\epsilon = -5k_{\mathrm{B}}T$ that is employed throughout the main article. The line for $\eta = \eta_{\mathrm{water}}$ is also shown in Fig. 5 (a) of the main article.

Figure S8 shows the viscosity dependence of slip velocities predicted by the uniform viscosity model of Derjaguin, Anderson, Prieve, Marbach and others (10, 12, 13) for a linear gradient formed between reservoirs at concentrations $c_0 = 0$ and Δc. These data are calculated according to Equations 2 and 3 in the main article text, using the square-well-like attractive surface-solute interaction of depth $\epsilon = -5k_{\mathrm{B}}T$ that has been employed throughout the main article. In this model, there is no increase in viscosity in the surface layer compared to the bulk and the predicted DO slip velocity consequently increases linearly with the concentration gradient, with a gradient that is inversely proportional to the (uniform) solution viscosity. Thus, for a given Δc, a higher viscosity results in a lower predicted slip velocity, but the linear increase in u_s with Δc is preserved for all η. In (a), data are shown in the semi-logarithmic representation used in Fig. 5 (a) of the main article. In (b) the same data are shown with a linear x axis.

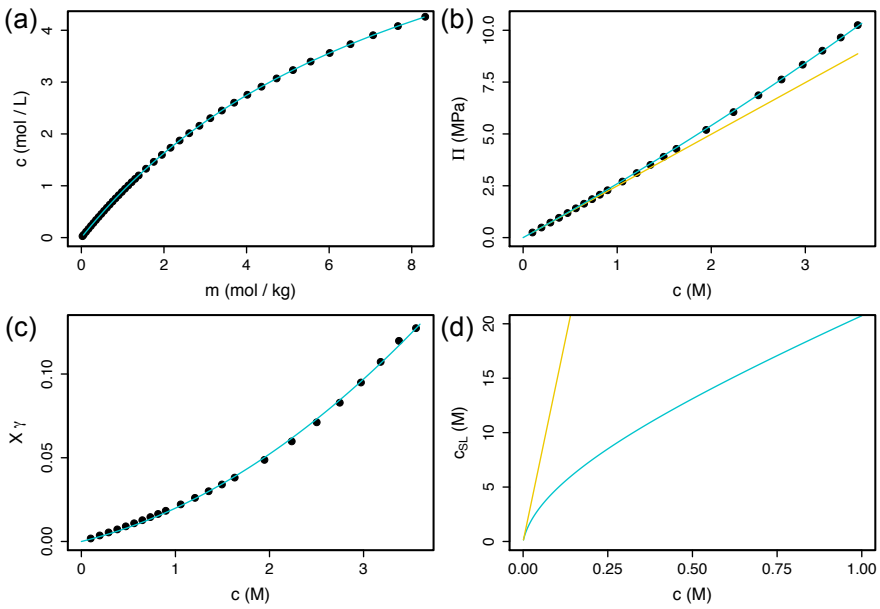

Fig. S9. (a) Aqueous glucose solution molarity (moles per litre of solution) as a function of molality (moles per kg of solvent). Black points are data from the CRC Handbook of Physics and Chemistry (6), line is linear interpolation between points. (b) Osmotic pressure of glucose solutions as a function of molarity. Black points are data from Miyajima *et al.* (11). Turquoise line is quadratic fit to these data. Gold line is the ideal solution osmotic pressure. (c) The product of mole fraction, X, and activity coefficient, γ, for glucose solutions. Black points are data from Miyajima *et al.* (11). Line is quadratic fit to data. (d) Dependence of surface layer concentration, c_{SL}, on bulk concentration, c, with $\epsilon = -5\,k_{\mathrm{B}}T$. Gold line shows ideal solution relationship, turquoise line shows the result of quadratic corrections for a non-ideal solution.

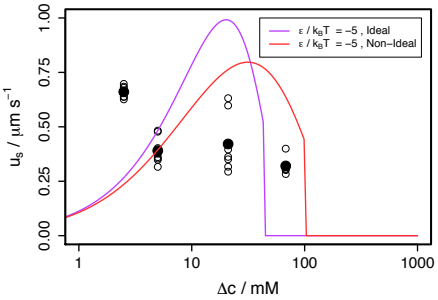

Fig. S10. Comparison of experimental estimates of slip velocity (points) with model predictions in glucose gradients between reservoirs at $c_0 = 0$ and Δc. Solid black points are average over repeated experiments, open circles are individual experiments. Purple line is model prediction for $\epsilon = -5\,k_{\mathrm{B}}T$ using ideal solution expressions for c_{SL} and Π as described in the main manuscript. Red line shows refined model predictions with $\epsilon = -5\,k_{\mathrm{B}}T$ and using quadratic order corrections to c_{SL} and Π for non-ideal solutions.

Here we refine our model to account for non-ideal effects in aqueous glucose solutions. The model as presented in the main manuscript assumes an ideal solution, for which osmotic pressure is $\Pi_0 = cN_{\mathrm{A}}k_{\mathrm{B}}T/10^{-3}$ and the relationship between bulk and surface layer concentrations is $c_{\mathrm{SL}} = c\exp\left(-\epsilon/k_{\mathrm{B}}T\right)$. Here we correct both these relationships to order c^2 using experimental measurements osmotic and activity coefficients for aqueous glucose solutions reported by Miyajima *et al.* (11).

Miyajima and coworkers report their data in terms of molality (moles per kg of solvent) and so we first map molality to molarity (moles per litre of solution, refered to as concentration throughout this article) using data from the CRC Handbook of Physics and Chemistry (6). Molarity as a function of molality for glucose solutions are shown in Fig. S9 (a), where the line is a linear interpolation between the points. This interpolation is used to map Miyajima's data from molality to molarity.

The first correction to the ideal solution model is in the dependence of osmotic pressure on concentration. Figure S9 shows the ideal solution osmotic pressure, $\Pi_0 = cN_{\mathrm{A}}k_{\mathrm{B}}T/10^{-3}$, as a gold line. Experimental measurements (11) are shown as black points. These are fit with a quadratic function of the form $\Pi = (c + A_{\Pi}c^2)(N_{\mathrm{A}}k_{\mathrm{B}}T/10^{-3})$, where the fit parameter is $A_{\Pi} = 0.0422\,\mathrm{M}^{-1}$.

The relationship between surface layer and bulk concentration is found by replacing the ideal solution relationship $c_{\mathrm{SL}} = c \exp(-\epsilon/k_{\mathrm{B}}T)$ with

$$X(c_{\mathrm{SL}})\gamma(c_{\mathrm{SL}}) = X(c)\gamma(c)\exp(-\epsilon/k_{\mathrm{B}}T), \quad [13]$$

where $X(c)$ is the mole fraction of a solution at concentration c and $\gamma(c)$ is the corresponding activity coefficient. The dependence of the product $X\gamma$ on c is shown in Fig. S9 (c), where black points are data from Miyajima *et al.* (11) and the line is a quadratic fit to these data of the form $X\gamma = Ac + Bc^2$. The fit parameters are $A = 0.0137$ and $B = 0.00621$.

For a given bulk concentration, c, Eq. 13 yields a quadratic equation for c_{SL}, the positive root of which is surface layer concentration in this refined model. The relationships between c and c_{SL} are shown in Fig. S9 (d) for an ideal solution (gold line) and with our quadratic refinement (turquoise line).

Numerically calculating the diffusioosmotic velocity using these new relationships, and calculating the gradient $\partial_x(\Pi_{\mathrm{SL}} - \Pi_{\mathrm{bulk}})$ locally yields predictions for DO slip velocity as a function of Δc as indicated by the red line in Fig. S10. The effect of applying quadratic corrections to the ideal solution expressions is to reduce the maximum slip velocity, broaden the peak and shift it to larger Δc.

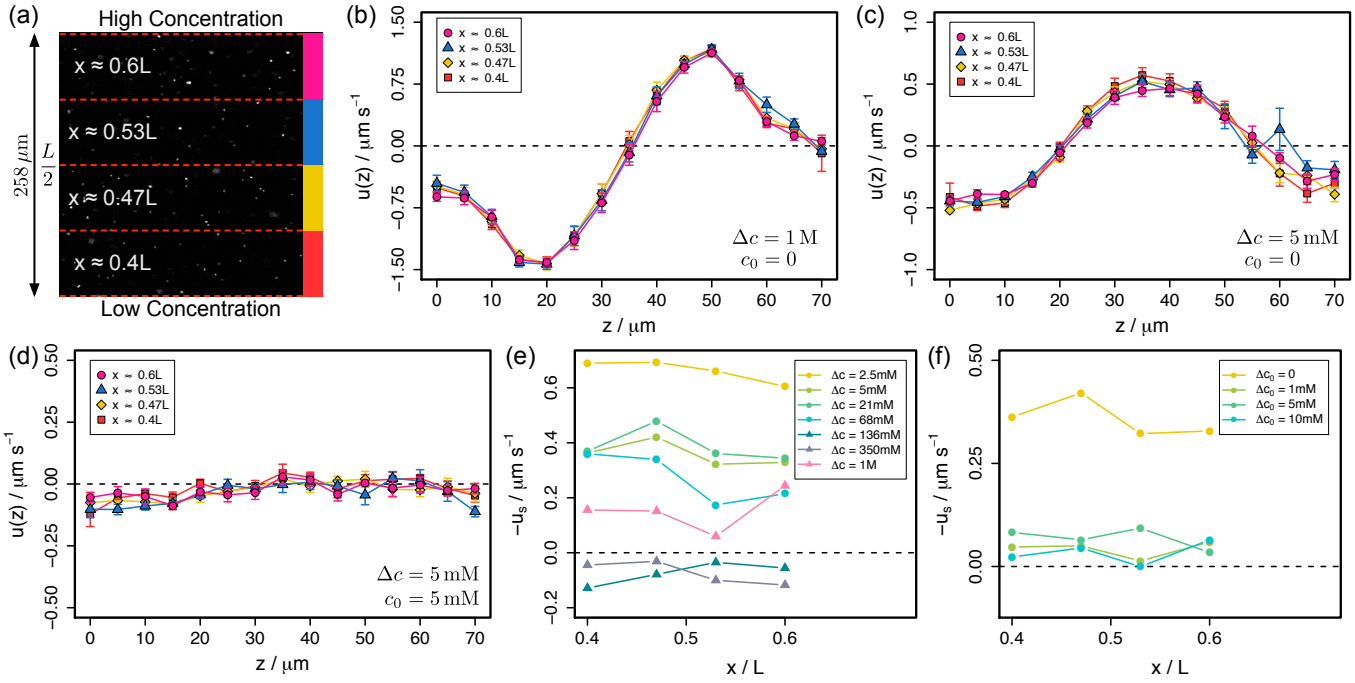

Fig. S11. (a) Schematic illustrating dividing experimental data into 4 subregions. Images extend $258\,\mu$m along the gradient direction and are centred at $L/2$. Due to the gradient, glucose concentration is greater at the top of the image than at the bottom. Here the data are subdivided into 4 subregions centred at $x \approx 0.4L$, $0.47L$, $0.53L$ and $0.6L$. (b-d) Comparison of average velocity profiles calculated in the subregions identified in (a). Data are coloured according to the subregion. Error bars represent the standard error of the mean. Δc and c_0 are indicated in the lower right of each panel. (e) & (f) Position dependence of estimated slip velocity when (e) background concentration $c_0 = 0$ and when (f) $\Delta c = 5\,\mathrm{mM}$. In (e), circular points represent slip-velocity-driven flows and triangular points represent convective flows.

Our experimental measurements suggest that the fluid velocity profile and DO slip velocity depend on both the glucose concentration gradient and the glucose concentration. Experimental measurements are not made at a single location, but are the spatial average over images that span $258\,\mu$m of the channel centred at the channel centre, $x = L/2$. Therefore, the glucose concentration near the top of the image is larger than the concentration near the bottom of the image.

Instead of performing the spatial averaging over the entire image, we can instead divide the image into horizontal strips and define 4 subregions as indicated in Fig. S11 (a). In this way, we measure velocity profiles centred around four different locations ($x \approx 0.4L$, $0.47L$, $0.53L$ and $0.6L$) and can assess whether these profiles depend on position, within the limits of our experimental data. Splitting the data into subregions reduces the number of particles in each region, compared to the whole image, and so averages are performed over fewer particle displacements. As a result, statistics suffer and the extracted profiles become less indicative of average behaviour. We find that 4 is the maximum number of subregions into which we can divide our data while retaining acceptable velocity profiles.

Figure S11 (b-d) show the average velocity profiles measured in the 4 subregions under 3 experimental conditions. The data are coloured according to the subregion as indicated in the legends and in (a). Data in (b) show experiments with $\Delta c = 1\,\mathrm{M}$ and $c_0 = 0$ in which flow is convection-dominated. Data in (c) show experiments with $\Delta c = 5\,\mathrm{mM}$ and $c_0 = 0$ in which flow is DO-dominated. Data in (d) show experiments with $\Delta c = 5\,\mathrm{mM}$ and $c_0 = 5\,\mathrm{mM}$ in which flow is suppressed. We observe no significant differences between the profiles obtained in these subregions under any of our experimental conditions. This does not mean that flow profiles are independent of position throughout the entire channel, just that we cannot resolve any position dependence in the region close to channel centre where our data are acquired.

Figure S11 (e) and (f) show the estimated average slip velocities extracted from the velocity profiles measured in each of the subregions, visualised as a function of x position between $0.4L$ and $0.6L$. In (e), circular points represent slip velocity driven flow profiles and triangular points show convection dominated profiles. These data are by no means conclusive, but do hint at a decrease in slip velocity at larger x in the experiments which undergo slip velocity driven flow [circles in (e) and yellow data in (f)]. More extensive experiments exploring a larger range of positions are really required to fully investigate this effect.

Within the experimental observation region, any position dependence in the velocity profiles is too weak to have significant impact on our measurements.

The Effect Of Non-Uniform Slip Velocity On Observed Velocity Profiles. As we have no net flow, either in x (along the channel) or z (vertical direction), we have the familiar problem of flow in a cavity, *i.e.*, in a closed box. This is also called simple contained flow, where the normal component of the velocity is zero everywhere along the boundary (14). For convenience we work in two dimensions, and assume the fluid is incompressible. Thus our problem is a two-dimensional cavity flow problem, with the slip velocities due to DO appearing as fixed boundary conditions on the flow velocity along x at the bottom and top walls.

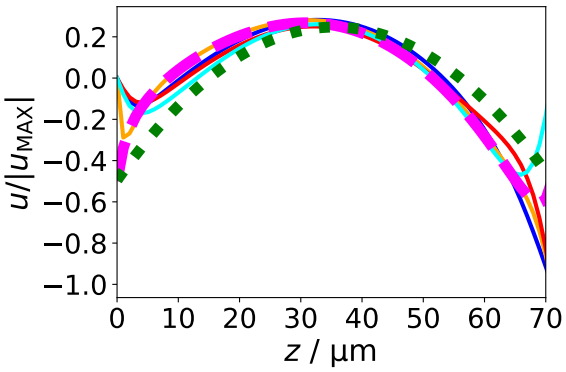

Fig. S12. The x component of the flow velocity as a function of height z, obtained by two-dimensional Navier-Stokes simulations with patchy slip velocities along the top and bottom walls. The patch size is 5 μm. Other than the patch size the simulation is the same as in Fig. 5 (c) of the main text. The thick green dotted curve is the analytic prediction for uniform slip velocity ($u_{\rm MAX}/2$) given in Eq. 4 of the main text. The thick dashed magenta curve is the profile averaged over 10 μm along x, *i.e.*, over two patches. The thinner solid curves are local profiles at single x positions, *i.e.*, not averaged along the x axis.

To solve the Navier-Stokes equations for two-dimensional cavity flow we follow Hau and Ohl's modification (15) of Barba and Forsyth (16)'s Navier-Stokes code, which is a Jupyter Python notebook. Our code is just a small modification (of the boundary conditions) of the Jupyter notebook for cavity flow of Hau and Ohl. The equations for cavity flow $\vec{u}$ of an incompressible fluid in two dimensions (x along the capillary, and z height in capillary) are (14) the Navier-Stokes equation

$$\frac{\partial \vec{u}}{\partial t} + (\vec{u}\cdot\nabla)\vec{u} = -\frac{1}{\rho}\nabla p + \nu\nabla^2\vec{u} \qquad [14]$$

together with a Poisson equation for the pressure that enforces $\nabla\cdot\vec{u}=0$. The Poisson equation we solve is

$$\begin{aligned}\nabla^2 p &= \frac{\rho}{\Delta t}\left[\frac{\partial u_x}{\partial x}+\frac{\partial u_z}{\partial z}\right] \\ &- \rho\left[\left(\frac{\partial u_x}{\partial x}\right)^2 + 2\frac{\partial u_x}{\partial z}\frac{\partial u_z}{\partial x} + \left(\frac{\partial u_z}{\partial z}\right)^2\right]\end{aligned} \qquad [15]$$

Note that the code we use to solve the Poisson equation for the pressure does not assume, that $\nabla\cdot\vec{u}$ is zero. In this we follow Hau and Ohl (15).

We set the mass density $\rho=1$. For incompressible flows, ρ simply sets the units for the pressure. Here ν is the kinematic viscosity. We set $\nu = 1$ μm$^2/\mu$s — we work with units of μm and μs.

Boundary conditions. The (Dirichlet) boundary conditions on the velocity are as follows. On all four sides, the component of the velocity normal to the surface, is zero. The parallel component is zero along sides at the left and right ends. Along the bottom and top edges, the parallel velocity component is set to the desired DO slip velocity profile.

For the pressure, we set the normal derivatives of p to (15)

$$\frac{\partial p}{\partial x} = \rho\nu\frac{\partial^2 u_x}{\partial x^2} \qquad x = \text{constant edges} \qquad [16]$$

and

$$\frac{\partial p}{\partial z} = \rho\nu\frac{\partial^2 u_z}{\partial z^2} \qquad z = \text{constant edges} \qquad [17]$$

i.e., a Neumann boundary condition (14).

Our cavity is 1000 by 70 μm, and the lattice constant for our square lattice is 1 μm, so we have 1001 by 71 lattice points. This lattice constant sets the minimum lengthscale for the heterogeneity in the slip velocity. For simplicity we just consider surfaces that are random arrays of patches all of fixed length $l_{\rm PATCH}$, with each patch having a 50 % probability of having a slip velocity $u_{\rm MAX} = -10^{-4}\mu$m/s, and a 50 % probability of having a slip velocity of zero. Thus the average slip velocity is $u_{\rm MAX}/2$. This value for $u_{\rm MAX}$ results in a Reynolds number defined by Re$=|u_{\rm MAX}|H/\nu = 7\times10^{-3}$, so we are in the Stokes-flow limit of low Reynolds number.

Results. Once the boundary conditions are set the Jupyter notebook is run for long enough that the flow field is only changing very slowly with time. We then take that to be the steady-state flow field.

In Fig. 5 (c) and in Fig. S12, we have plotted velocity profiles analogous to the experimental profiles in Fig. 3(a) of the main paper. This is for systems with patch sizes of 5 μm (Fig. S12) and 1 μm (Fig. 5 (c) in the main text). Comparing the dashed magenta and dotted green curves shows that averaging the flow velocity along the capillary produces profiles that are almost indistinguishable from those predicted by Eq. 4 of the main text for a uniform slip velocity of $u_{\mathrm{MAX}}/2$.

Local profiles at particular values of x (the thinner solid curves) start and end at the local slip velocity but relax to the average profile over a range that is approximately twice the patch size. We conclude that variations about a mean slip velocity of a characteristic size l_{PATCH} only propagate a few times l_{PATCH} into the fluid. Beyond this, the fluid velocity profile is almost indistinguishable from that expected for a uniform slip velocity along the surface. Essentially, the lengthscales of the variations in $\vec{u}$ along x and along z are comparable.

In these calculations the patches are restricted to be micrometre sized due to the constraint of our lattice, but we expect that any surface heterogeneity in our experimental system to be on nanometre lengthscales. We measure flow by tracking micrometre-sized colloidal particles in a sequence of videos spaced by 5 μm in z. Therefore, our experiments are blind to any non-uniformity of the DO slip velocity on sub-micrometre lengthscales, and sensitive only to the spatially-averaged slip velocity.

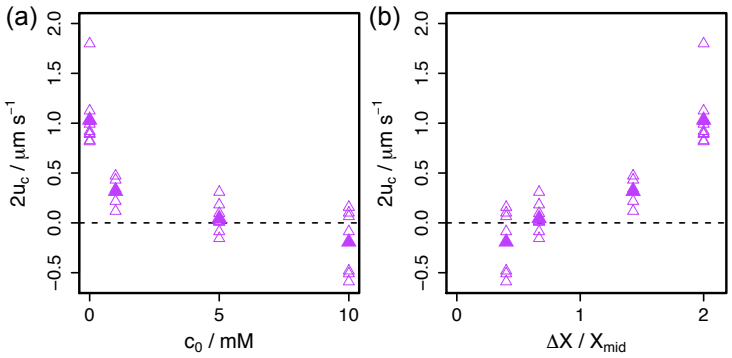

Fig. S13. (a) Twice the experimentally measured centre velocities (average tracer velocity in optical section at $z = H/2 = 35\,\mu$m) as a function of concentration in the low concentration reservoir, c_0, in the series of experiments with fixed gradient $\Delta c = 5\,$mM and increasing c_0. (b) Same data as (a) shown as a function of $\Delta X/X_{\rm mid}$, where ΔX is the difference in mole fraction between the reservoirs and $X_{\rm mid}$ is mole fraction at the channel centre. Open points are individual experiments and solid points show the average over all experiments at each c_0.

The analytical parabolic form for slip velocity driven flow (Eq. 4 in the main article) predicts that the magnitude of the fluid velocity at the channel centre, $z = H/2$, is half the slip velocity at the walls. Therefore, if experimentally measured flow profiles were to perfectly follow this parabolic shape, this provides an alternative method to estimate the slip velocity. However, as discussed in the main article, our slip velocity driven flow profiles *do not* exhibit this perfectly parabolic shape, and instead flatten off near the walls, meaning that the true slip velocity is smaller than would be estimated by measuring the centre velocity alone. Therefore, we believe that the centre velocity, u_c, may be an unreliable estimate of the slip velocity, u_s.

Nonetheless, for completeness, the centre velocities measured in experiments in fixed gradients formed between reservoirs at c_0 and $c_0 + 5\,$mM are shown as a function of c_0 in Fig. S13 (a). This figure should be directly compared with Fig. 4 (b) of the main article. Figure S13 (b) shows the same data as a function of $\Delta X/X_{\rm mid}$, where ΔX is the difference in mole fraction between the reservoirs and $X_{\rm mid}$ is mole fraction at the channel centre. This should be compared to the inset to Fig. 4 (b) in the main article.

The centre velocity decreases as c_0 increases (or as $\Delta X/X_{\rm mid}$ decreases), indicating the suppression of circulating DO-driven flow upon increasing the background concentration. When shown as a function of $\Delta X/X$, u_c appears closer to linear than u_s [inset to Fig. 4 (b) in the main article], but it is important to highlight that the average centre velocity at $c_0 = 10\,$mM is slightly negative, suggesting a change in the direction of the slip velocity. If the slip velocity did indeed follow a $\nabla \ln X$ scaling, these data would be linear, but should pass through the origin, and not cross zero at finite $\Delta X/X$. This apparent change in direction is attributed to the experimental uncertainty, and we note that the scatter in these velocities around $u_c = 0$ is comparable to the scatter of z-averaged velocity shown in Fig. S2 (a). Therefore, we do not believe that these data indicate a linear increase in u_c (or u_s) with $\Delta X/X$ and maintain that the slip velocity in our system does not follow the $\nabla \ln X$ scaling that Paustian *et al.* observed for diffusiophoresis in ethanol gradients (1).

References

1. JS Paustian, et al., Direct measurements of colloidal solvophoresis under imposed solvent and solute gradients. *Langmuir* **31**, 4402–4410 (2015).
2. A Banerjee, I Williams, R Nery Azevedo, M Helgeson, TM Squires, Soluto-inertial phenomena: Designing long-range, long-lasting, surface-specific interactions in suspensions. *Proc. Natl. Acad. Sci. USA* **113**, 8612–8617 (2016).
3. D Florea, S Musa, J Huyghe, H Wyss, Long-range repulsion of colloids driven by ion exchange and diffusiophoresis. *Proc. Natl. Acad. Sci. USA* **111**, 6554–6559 (2014).
4. S Battat, J Ault, S Shin, S Khodaparast, H Stone, Particle entrainment in Dead-End pores by diffusiophoresis. *Soft Matter* **15**, 3879–3885 (2019).
5. N Shi, R Nery Azevedo, A Abdel-Fattah, T Squires, Diffusiophoretic focusing of suspended colloids. *Phys. Rev. Lett.* **117** (2016).
6. JR Rumble, *CRC Handbook of Chemistry and Physics*. (CRC Press), 100 edition, (2019).
7. JF Brady, Particle motion driven by solute gradients with application to autonomous motion: continuum and colloidal perspectives. *J. Fluid Mech.* **667**, 216 (2011).
8. RP Sear, PB Warren, Diffusiophoresis in nonadsorbing polymer solutions: The asakura-oosawa model and stratification in drying films. *Phys. Rev. E* **96**, 062602 (2017).
9. JL Anderson, Colloidal transport by interfacial forces. *Ann. Rev. Fluid Mech.* **21**, 61 (1989).
10. S Marbach, H Yoshida, L Bocquet, Osmotic and diffusio-osmotic flow generation at high solute concentration. i. mechanical approaches. *J. Chem. Phys.* **146**, 194701 (2017).
11. K Miyajima, M Sawada, M Nakagaki, Studies on aqueous solutions of saccharides. i. activity coefficients of monosaccharides in aqueous solutions at 25 c. *Bull. Chem. Soc. Jpn.* **56**, 1620 (1983).
12. BV Derjaguin, SS Dukhin, MM Koptelova, Capillary osmosis through porous partitions and properties of boundary layers of solutions. *J. Colloid Interf. Sci.* **38**, 584–595 (1972).
13. JL Anderson, ME Lowell, DC Prieve, Motion of a particle generated by chemical gradients part 1. non-electrolytes. *J. Fluid Mech.* **117**, 107–121 (1982).
14. PM Gresho, RL Sani, On pressure boundary conditions for the incompressible navier-stokes equations. *Int. J. Num. Meth. Fluids* **7**, 1111–1145 (1987).
15. TB Hau, CD Ohl, PyCFD: A Pythonic introduction to numerical techniques used in computational fluid dynamics (2015) http://cav2012.sg/cdohl/CFD_course/index.html.
16. LA Barba, GF Forsyth, CFD Python: the 12 steps to Navier-Stokes equations. *J. Open Source Educ.* **1**, 21 (2018).